




Nonspherical optomagnonic resonators for enhanced magnon-mediated optical transitions

E. Almpanis ^{1,2,*}, N. Papanikolaou ¹ and N. Stefanou ²

¹*Institute of Nanoscience and Nanotechnology, NCSR “Demokritos,” Patriarchou Gregorinou and Neapoleos Str., Ag. Paraskevi, GR-153 10 Athens, Greece*

²*Section of Condensed Matter Physics, National and Kapodistrian University of Athens, Panepistimioupolis, GR-157 84 Athens, Greece*



(Received 4 October 2021; revised 3 December 2021; accepted 7 December 2021; published 20 December 2021)

We study magnon-mediated optical transitions in micrometer-sized axially symmetric yttrium iron garnet (YIG) particles, which act as optomagnonic cavities, by means of electromagnetic calculations, treating the magneto-optical coupling to first order in perturbation theory, in the framework of a fully dynamic approach. Such particles with engineered shape anisotropy exhibit high-quality-factor Mie resonances in the infrared part of the spectrum, with a separation of few gigahertz, which matches the typical frequencies of magnons. This allows for optical transitions mediated by spin waves, while the micrometer volume favors stronger overlap between the optical modes and the precessing magnetization. Our results predict that photon-magnon coupling strengths of tens of kilohertz could be realized with cylindrical or spheroidal particles, since mainly the reduced volume, but also shape anisotropy, can lead to strong, up to four orders of magnitude, enhancement of the coupling strengths compared to submillimeter YIG spheres.

DOI: [10.1103/PhysRevB.104.214429](https://doi.org/10.1103/PhysRevB.104.214429)

I. INTRODUCTION

Photons and magnons are very promising information carriers, which can be handily manipulated through the development of structures such as photonic crystals [1,2] and magnonic crystals [3,4], respectively. What is more, visible/near-infrared (Vis/NIR) and telecommunication photons can efficiently transfer information between different parts of a large network using conventional technology, while magnons are very promising agents for data storage [3,5] and signal processing [6,7]. In view of these, controlling and enhancing the interaction between Vis/NIR light and spin waves would provide impressive opportunities in the development of magnon-based microwave-to-optical transducers [8,9] suitable for quantum-computing applications [10,11]. To this end, a new class of structures with dual optical and magnonic functionalities, so-called *optomagnonic* structures [12], emerged in recent years.

So far, several optomagnonic configurations have been proposed, including planar waveguides for microwave-to-optical conversion [13,14], hybrid photonic-magnonic crystals [15,16], Fabry-Pérot cavities [17–22], and optomagnonic beams [23]. However, millimeter-sized yttrium-iron-garnet (YIG) spherical resonators are yet the most typical examples of experimentally investigated optomagnonic cavities [24–26]. Such spherical resonators exhibit high- Q optical whispering gallery modes (WGM) in the Vis/NIR part of the spectrum while, at the same time, supporting magnons excited in the fundamental mode that corresponds to the uniform precession of the magnetization, usually termed Kittel mode [27], with frequencies of a few gigahertz. When the

magnon frequency matches the frequency difference between two successive WGMs, optical frequency up (down) conversion through a respective absorption (emission) of a magnon can be triggered, as has been verified by Brillouin light scattering experiments [24–26].

However, until now, the measured magnon-mediated photon-to-photon transition probabilities in spherical YIG resonators are rather small [8,24–26], which hinders the possibility for practical applications. A crucial limiting factor is the size of the spheres. Since millimeter-sized diameters correspond to rather small overlap between optical and spin modes, shrinking both the optical and magnetic mode volumes could enhance the optomagnonic coupling strength by orders of magnitude [28,29]. Yet, in spherical YIG microparticles, magnon-mediated optical transitions are not possible, since the separation between Mie modes is much larger than the magnon frequencies. This limitation is relaxed in nonspherical particles, that we consider here, where the anisotropy-induced splitting of the Mie resonances can be tuned in the GHz range so as to match the magnon frequencies in micrometer-sized YIG particles.

In spherical particles, optical modes are $(2\ell + 1)$ fold degenerate, while for axially symmetric particles, such as spheroids or cylinders, this degeneracy is lifted. Each mode can be assigned to a magnetic number $|m|$ and the angular momentum channels ℓ are mixed [30]. For a micron-sized sphere in the Vis/NIR, the frequency difference between two successive Mie modes is a few terahertz. By deviating from sphericity, one can control the separation of the modes and, for properly adjusted geometrical parameters, the spectral distance between two successive $|m|$ -split modes can reach the order of gigahertz, matching the typical frequencies of magnons. In a previous work [29], triply resonant photon transitions were studied in micron-sized magnetic spheres,

*ealmpanis@gmail.com

where mode splitting was controlled by the optical anisotropy induced by the Faraday coefficient. Nevertheless, the Faraday coefficient is a characteristic of the material and cannot be tuned at will. This limitation is severe since only Bi-or-Ce-doped garnet materials have a strong Faraday coefficient which, however, is accompanied by considerable material losses. On the contrary, in the present work, we propose that common undoped YIG particles can be geometrically engineered to obtain the desirable optical mode splitting.

In view of the above, in the present work, we report on the coupling between the Kittel magnon and optical Mie resonances inside an axially symmetric YIG particle, which acts as an optomagnonic cavity. We restrict ourselves in the weak-coupling regime, which is valid for YIG optomagnonic resonators [24–26], where magnon-mediated photon-to-photon transition probabilities can be evaluated to first-order Born approximation. This approach is sufficient for our purposes, while at the same time allowing for a deeper insight into the underlying physics. The remainder of the paper is organized as follows. In Sec. II we briefly outline the theoretical method employed for the calculation of the electromagnetic (EM) field eigenmodes of an axially symmetric particle and analyze the symmetry of these modes in terms of group theory. In Sec. III we discuss photon transitions between $|m|$ -split Mie modes, induced by the Kittel magnon, evaluated to first order in perturbation theory, and establish the selection rules that govern such transitions. In Sec. IV, which is devoted to the discussion of our results, we provide a consistent interpretation of the calculated photon transition amplitudes between different modes. The last section summarizes the main findings of the paper.

II. METHOD OF CALCULATION

The optical eigenmodes of the axially symmetric particles considered in this work are calculated by the extended-boundary-condition method (EBCM) [31,32]. Spherical wave expansions are used to describe the electric field inside and outside the particle. Let us consider a homogeneous particle with relative permittivity and permeability ϵ and μ , respectively, in a homogeneous host medium characterized by corresponding parameters ϵ_h and μ_h . For a time-harmonic, monochromatic EM wave, of angular frequency ω , the electric field can be written as $\mathbf{E}(\mathbf{r}, t) = \text{Re}[\mathbf{E}(\mathbf{r}) \exp(-i\omega t)]$ and, expanding into vector spherical waves about a given origin (at the center of the particle), we have

$$\mathbf{E}(\mathbf{r}) = \sum_{\ell=1}^{\infty} \sum_{m=-\ell}^{\ell} \left[\frac{i}{q_h} a_{E\ell m}^0 \nabla \times j_{\ell}(q_h r) \mathbf{X}_{\ell m}(\hat{\mathbf{r}}) + a_{H\ell m}^0 j_{\ell}(q_h r) \mathbf{X}_{\ell m}(\hat{\mathbf{r}}) \right], \quad (1)$$

where $q_h = \omega \sqrt{\epsilon_h \mu_h} / c$, c being the velocity of light in vacuum, j_{ℓ} are the spherical Bessel functions which are finite everywhere, and $\mathbf{X}_{\ell m}(\hat{\mathbf{r}})$ are the vector spherical harmonics. The expansion coefficients $a_{P\ell m}^0$, $P = E, H$, are associated with multipoles of electric and magnetic type, which are transverse magnetic (TM) and transverse electric (TE), respectively. For the field inside the particle, a similar expansion

as that of Eq. (1) can be used, with appropriate coefficients, $a_{P\ell m}^i$, and q_h replaced by $q = \sqrt{\epsilon \mu} \omega / c$. The scattered field is also expressed in the form of Eq. (1), by replacing the spherical Bessel functions, j_{ℓ} , with spherical Hankel functions, h_{ℓ}^+ , which are appropriate to outgoing spherical waves: $h_{\ell}^+(x) \approx (-i)^{\ell} \exp(ix) / ix$ as $x \rightarrow \infty$ and expansion coefficients $a_{P\ell m}^+$ [32].

The field expansion coefficients can be expressed in terms of those of the incident wave ($a_{P\ell m}^0$) through the scattering T matrix and Q matrix as follows:

$$a_{P\ell m}^+ = \sum_{P'\ell'm'} T_{P\ell m; P'\ell'm'} a_{P'\ell'm'}^0 \quad (2)$$

and

$$a_{P\ell m}^i = \sum_{P'\ell'm'} Q_{P\ell m; P'\ell'm'} a_{P'\ell'm'}^0. \quad (3)$$

To calculate the T and Q matrices for a nonspherical scatterer, we employ the EBCM, which takes into account the continuity of the tangential components of the EM field on the surface of the scatterer through appropriate surface integrals [31,32]. Although the spherical-wave expansions of the EM field are infinite series, it turns out that, if the size of the particle is comparable to the wavelength, a limited number of partial waves, corresponding to $\ell \leq \ell_{\max}$, is sufficient for the description of the field inside and outside the particle. Nevertheless, an accurate calculation of the T and Q matrices requires elements up to $\ell_{\text{cut}} \geq \ell_{\max}$. We note that ℓ_{cut} increases as we deviate from sphericity. However, when the aspect ratio of an axisymmetric particle does not strongly deviate from unity, as in the cases considered here, excellent convergence is obtained using a moderate number of spherical harmonics [30–34].

The eigenmodes of a particle are obtained in the absence of an incoming wave. In general, a single particle supports resonant modes of the EM field at the poles of the eigenvalues of the T matrix, which are complex eigenfrequencies, $z_{\nu} = \omega_{\nu} - i\gamma_{\nu}$, $\nu = 1, 2, \dots$, with ω_{ν} being the resonance frequency and γ_{ν} / π the corresponding resonance linewidth, since the modes are not completely bound. Causality implies $\gamma_{\nu} > 0$ for the assumed $\exp(-i\omega t)$ time dependence. The field distributions for each eigenmode are retrieved from the corresponding eigenvectors, which provide the unknown field expansion coefficients.

In the case of axially symmetric particles which have a mirror plane normal to the symmetry axis, such as spheroids, cylinders, etc., the eigenmodes can be computed separately for every different value of $|m|$ and parity $\sigma = g$ (*gerade*) or $\sigma = u$ (*ungerade*) of the spherical vector wave function, which remain constant because of the symmetry of the system. Therefore, in each $|m|\sigma$ invariant subspace, we use the index $\nu = 1, 2, \dots$ to label the successive solutions. In terms of group theory, the $(2\ell + 1)$ degeneracy of a Mie mode in a spherical particle is (partially) lifted when the shape of the particle becomes spheroidal or cylindrical, say, with the symmetry axis along the z direction, because the symmetry is reduced from $O(3)$ to $D_{\infty h}$ [35]. Projecting onto the irreducible representations of the $D_{\infty h}$ point group, listed in Table I, one obtains $|m| = 0, 1, \dots, \ell$ distinct modes. These modes, for $m = 0$, are nondegenerate and have the symmetry

TABLE I. Character table of the $D_{\infty h}$ point group ($n = 1, 2, 3, \dots$). C_ϕ are rotation operations through an angle ϕ ($0 < \phi \leq \pi$ and $-\pi < \phi < 0$) about the symmetry axis (z), $C_{2'}$ are rotations through π about axes lying in the x - y plane, and I is the inversion operation.

$D_{\infty h}$	E	$2C_\phi$	$C_{2'}$	I	$2IC_\phi$	$IC_{2'}$
A_{1g}	1	1	1	1	1	1
A_{1u}	1	1	1	-1	-1	-1
A_{2g}	1	1	-1	1	1	-1
A_{2u}	1	1	-1	-1	-1	1
E_{ng}	2	$2 \cos(n\phi)$	0	2	$2 \cos(n\phi)$	0
E_{nu}	2	$2 \cos(n\phi)$	0	-2	$-2 \cos(n\phi)$	0

of the one-dimensional irreducible representations A_{1g} , A_{1u} , A_{2g} , and A_{2u} , for a TM (electric) multipole of even order, a TE (magnetic) multipole of even order, a TE (magnetic) multipole of odd order, and a TM (electric) multipole of odd order, respectively. For $m \neq 0$, the modes are doubly degenerate and have the $E_{|m|g}$ symmetry for a TM multipole of even order or a TE multipole of odd order, and the $E_{|m|u}$ symmetry for a TM multipole of odd order or a TE multipole of even order [30]. This means that each $|m|$ -split Mie mode is characterized by a well-defined value of $|m|$, while these modes have the same parity σ and order ν , namely those of the degenerate parent Mie modes of the sphere. Consequently, they have neither a specific polarization nor a specific multipole order in the strict sense, though their dominant character is that of the parent Mie modes.

III. MAGNON-INDUCED PHOTON TRANSITIONS

We will consider nonspherical axially symmetric, oblate, and prolate spheroidal as well as cylindrical particles that exhibit $|m|$ -split optical Mie resonances. For such a magnetic particle, magnetized to saturation (M_s) along its axis of revolution (taken along the z direction), we assume that the magnetization $\mathbf{M}(t)$ is precessing in phase about the z axis throughout the entire particle (Kittel magnon [36])

$$\mathbf{M}(t)/M_s = \eta \cos(\Omega t) \hat{\mathbf{x}} + \eta \sin(\Omega t) \hat{\mathbf{y}} + \hat{\mathbf{z}}, \quad (4)$$

where Ω is the magnon angular frequency, while the precession angle is $\vartheta = \arctan(\eta)$ [28].

The resulting permittivity can be written as a static and a time-dependent dynamic part, in the following tensor form:

$$\bar{\epsilon}(t) = \bar{\epsilon} + \delta\bar{\epsilon}(t), \quad (5)$$

while the permeability is assumed to be equal to unity ($\mu = 1$). Generally, both the static and dynamic parts of the permittivity are tensors [29]. However, as detailed by Zouros *et al.* [37] in the low magneto-optical coupling limit, when the dimensionless Faraday coefficient $f \ll 1$, the frequency shift of the optical eigenmodes caused by the static magnetization is negligibly small. Therefore, we ignore the influence of the static magnetization on the permittivity and assume that the static tensor permittivity $\bar{\epsilon} \rightarrow \epsilon \bar{I}$, where \bar{I} is the unit tensor and ϵ is the scalar permittivity of the unmagnetized particle. The magnon-mediated optical transitions arise from the dynamic part in Eq. (5). In our case, the time-dependent part of

the permittivity reads [29]

$$\delta\bar{\epsilon}(t) = \begin{pmatrix} 0 & 0 & -if\eta \sin(\Omega t) \\ 0 & 0 & if\eta \cos(\Omega t) \\ if\eta \sin(\Omega t) & -if\eta \cos(\Omega t) & 0 \end{pmatrix}. \quad (6)$$

In the weak-coupling regime [8,17,24–26,38,39], we use the first-order Born approximation and the magnon-mediated transitions are described by the overlap integral $G = \langle f | \delta\bar{\epsilon} | i \rangle$, where $\langle \alpha \mathbf{r} \mathbf{r} | i \rangle = E_{i,\alpha}(\mathbf{r}) \exp(-i\omega_i t)$ and $\langle f | \alpha \mathbf{r} \mathbf{r} \rangle = E_{f,\alpha}^*(\mathbf{r}) \exp(i\omega_f t)$, with α denoting (Cartesian) component, correspond to appropriate initial (i) and final (f) EM modes of the unmagnetized particle. As discussed in the previous section, quite generally, these modes are labeled by indices $m_i \sigma_i \nu_i$ and $m_f \sigma_f \nu_f$, respectively. The overlap integral reads [29]

$$G = \pi [\delta(\omega_i - \omega_f + \Omega) g_+ + \delta(\omega_i - \omega_f - \Omega) g_-], \quad (7)$$

where

$$g_\pm = if\eta (\hat{\mathbf{x}} \pm i\hat{\mathbf{y}}) \cdot \int_V d^3r \mathbf{E}_f^*(\mathbf{r}) \times \mathbf{E}_i(\mathbf{r}), \quad (8)$$

with the star denoting complex conjugation. The delta functions in Eq. (7) express energy conservation in the optical transitions that involve absorption and emission of one magnon by a photon, as expected in the linear regime. The volume integral in Eq. (8) is performed in a spherical (r, θ, ϕ) coordinate system, where the ϕ integration is carried out analytically.

The spin wave amplitude η is normalized so as to correspond to a single magnon within the volume of the particle V , through the relation

$$\eta = \sqrt{\frac{2\hbar|\gamma_e|}{M_s V}}, \quad (9)$$

where γ_e is the gyromagnetic ratio and the quantity $\hbar|\gamma_e|$ corresponds to one Bohr magneton [40,41]. We note that, even for cylindrical particles, assuming a uniform spin-wave amplitude distribution is a reasonable approximation when the aspect ratio is close to unity [39]. Similarly, the photonic eigenmodes $|s\rangle$ ($|i\rangle$ or $|f\rangle$) are normalized so as to correspond to a single photon [39]

$$\frac{1}{4} \int_V d^3r [\mathbf{E}_s(\mathbf{r}) \cdot \mathbf{D}_s^*(\mathbf{r}) + \mathbf{H}_s(\mathbf{r}) \cdot \mathbf{B}_s^*(\mathbf{r})] = \frac{\hbar\omega_s}{2}. \quad (10)$$

Let us now apply symmetry arguments to extract the allowed photon-to-photon transitions in such processes. It can be shown [29] that $\delta\bar{\epsilon}$ and $\delta\bar{\epsilon}^\dagger$ are irreducible tensor operators, which have the symmetry of the two-dimensional irreducible representation E_{1g} of $D_{\infty h}$. Therefore, $\delta\bar{\epsilon}$ or $\delta\bar{\epsilon}^\dagger$, operating on an eigenvector of the $|m|\sigma$ irreducible subspace, transforms according to the relevant direct product representation

$$\begin{aligned} E_{1g} \otimes A_{1\sigma} &= E_{1\sigma}, \quad E_{1g} \otimes A_{2\sigma} = E_{1\sigma}, \quad \text{if } m = 0, \\ E_{1g} \otimes E_{1\sigma} &= E_{2\sigma} \oplus A_{1\sigma} \oplus A_{2\sigma}, \quad \text{if } |m| = 1, \\ E_{1g} \otimes E_{|m|\sigma} &= E_{(|m|+1)\sigma} \oplus E_{(|m|-1)\sigma}, \quad \text{if } |m| \geq 2, \end{aligned} \quad (11)$$

where $\sigma = g$ or $\sigma = u$. These considerations imply simple selection rules for the above photon transitions: $|m_f| = |m_i| \pm 1$

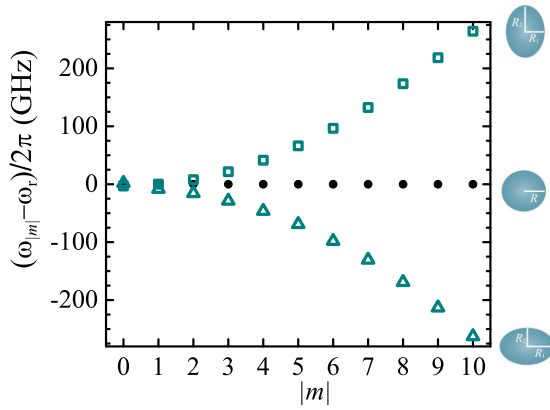


FIG. 1. Eigenfrequencies of $|m|$ -split Mie modes of unmagnetized YIG spheroidal particles: an oblate spheroid of radii $R_1 = 5.1 \mu\text{m}$, $R_2 = 4.9 \mu\text{m}$ (triangular open symbols) and a prolate spheroid of radii $R_1 = 4.9 \mu\text{m}$, $R_2 = 5.1 \mu\text{m}$ (square open symbols). The black solid circles show the eigenfrequency, ω_r , of the corresponding degenerate Mie modes ($\text{TM}_{\ell=10, v=1}$) of a sphere with radius $R = 5 \mu\text{m}$, which serves as a reference for the visualization of level splitting in the GHz scale.

for one-magnon absorption (anti-Stokes) and one-magnon emission (Stokes) processes, while both initial and final states must have the same parity, $\sigma_f = \sigma_i$. As long as in the present work we are concerned with transitions between $|m|$ -split Mie modes, which have the same parity σ and order v (those of the parent Mie modes), we shall denote each of the initial and final states by a single index, m_i and m_f , respectively. We note in passing that, for YIG resonators, the Kittel magnon decay rate, γ_K , is at the order of MHz [24–26], while the photon decay rates, γ_v , for the Mie modes assumed here are at the order of GHz. This allows us to neglect magnon lifetime effects while taking into account the finite radiative lifetime of the photon modes in the description of the triply resonant transition.

IV. RESULTS AND DISCUSSION

At first, we consider two different micrometer-sized YIG spheroidal particles in air, one prolate and one oblate, of similar volumes, that operate as optomagnonic resonators. The prolate spheroid has radii $R_1 = 4.9 \mu\text{m}$ and $R_2 = 5.1 \mu\text{m}$, while the oblate one has radii $R_1 = 5.1 \mu\text{m}$ and $R_2 = 4.9 \mu\text{m}$ (see Fig. 1). Such dielectric magnetic particles, of micron or submicron size, can be fabricated by various techniques [42–46]. In general, YIG microparticles support complex-frequency eigenmodes of the EM field, as discussed in Sec. II, which can be excited either by free-wave coupling (scattering configuration) [28], evanescent coupling [24,25], or fluorescence coupling [47]. We assume a relative magnetic permeability equal to unity and an electric permittivity $\epsilon = 4.84$, while the dimensionless Faraday coefficient is taken $f = -0.0005$, as appropriate for YIG in the infrared part of the spectrum where dissipative losses are negligibly small [36]. In the calculations, we truncated the angular-momentum expansions at $\ell_{\text{max}} = 13$, $\ell_{\text{cut}} = 16$, and used a Gaussian quadrature integration formula with 1024 points for the integrals involved, which ensures well converged results.

To understand the influence of deviating from the spherical shape, we start with a spherical particle, of almost the same size, which supports long-lifetime, spectrally separated, multipole (2^ℓ -pole) Mie resonances of TM or TE type, which confine the field inside the particle. Here, we choose such a particular resonance, namely the $\text{TM}_{\ell=10, v=1}$ one, located at a frequency $\omega_r/2\pi = 63.438 \text{ THz}$, i.e., a free-space wavelength equal to $4.725 \mu\text{m}$. This resonance corresponds to $2\ell + 1 = 21$ degenerate m modes at the same frequency, as shown with solid dots in Fig. 1. For the oblate or prolate spheroidal particle, the corresponding $|m|$ -split modes are being distinguished at different frequencies, as shown with open symbols in Fig. 1, with their calculated linewidth γ/π being about 3 GHz, which indicates the existence of high- Q spectrally separated resonances. The separation between successive ($\Delta|m| = \pm 1$) modes varies roughly from 10 GHz to about 50 GHz, which lies within the frequency range of Kittel modes in YIG resonators [24–26]. It is also worth noting that the $|m|$ -mode frequency separation can be precisely controlled by the aspect ratio (R_2/R_1) of the spheroid.

We now calculate the transition amplitude upon one-magnon absorption, g_+ , given by Eq. (8), between two successive initial, $|i\rangle = \sin \varphi_i | -m_i \rangle + \cos \varphi_i | m_i \rangle$, and final, $|f\rangle = \sin \varphi_f | -m_f \rangle + \cos \varphi_f | m_f \rangle$, $|m|$ -split Mie modes complying with the selection rule $|m_f| = |m_i| \pm 1$, assuming that the magnon frequency fulfills the triple-resonance condition $\omega_f = \omega_i + \Omega$, as schematically depicted in Fig. 2(a). The spin-wave amplitude is $\eta \simeq 7.1 \times 10^{-7}$ for the prolate and $\eta \simeq 6.9 \times 10^{-7}$ for the oblate spheroid, as obtained from Eq. (9) substituting the gyromagnetic ratio $|\gamma_e|/2\pi = 28 \text{ GHz/T}$ and the saturation magnetization $M_s = 140 \text{ kA/m}$ for YIG [36,39]. The results for the optomagnonic coupling strength $\tilde{g}_+ \equiv \epsilon_0 |g_+|/\hbar$ (ϵ_0 is the vacuum permittivity) for triple-resonant photon transitions from an initial photon state in the irreducible subspace with $|m_i| = 9$ to a final photon state in the irreducible subspace with $|m_f| = 10$ for the prolate spheroid under consideration are shown in Fig. 2(b). Similarly, in Fig. 2(c) we show the respective values \tilde{g}_+ for the oblate spheroid that correspond to triple-resonant photon transitions from an initial photon state in the irreducible subspace with $|m_i| = 10$ to a final photon state in the irreducible subspace with $|m_f| = 9$. Both cases have maximum \tilde{g}_+ at $\varphi_i = \pm \varphi_f = \pm \pi/4$.

Every value of g_+ can be calculated as a linear combination of four basic matrix elements between $|m_i\rangle$, $| -m_i \rangle$ and $|m_f\rangle$, $| -m_f \rangle$. In other words, we only need to numerically calculate g_+ for $\varphi_i = 0, \pi/2$ and $\varphi_f = 0, \pi/2$. We also note that one of the aforementioned transitions, which correspond to either $\varphi_i = 0$ and $\varphi_f = 0$ or $\varphi_i = \pi/2$ and $\varphi_f = \pi/2$ (depending if we have magnon absorption or emission), is also allowed for a spherical particle, where it can be analytically calculated using closed form relations [29]. Those analytically calculated values for a sphere with radius $R = 5 \mu\text{m}$ are very close to the respective values of the given spheroids. On the other hand, transitions from $\varphi_i = 0$ to $\varphi_f = \pi/2$ or from $\varphi_i = \pi/2$ to $\varphi_f = 0$ are not allowed in the sphere, because they are forbidden by symmetry [29]. Therefore, an analytic approximation using closed form relations is not possible, even for such very-close-to-spherical resonators. Furthermore, the maximum \tilde{g}_+ is obtained for combinations between

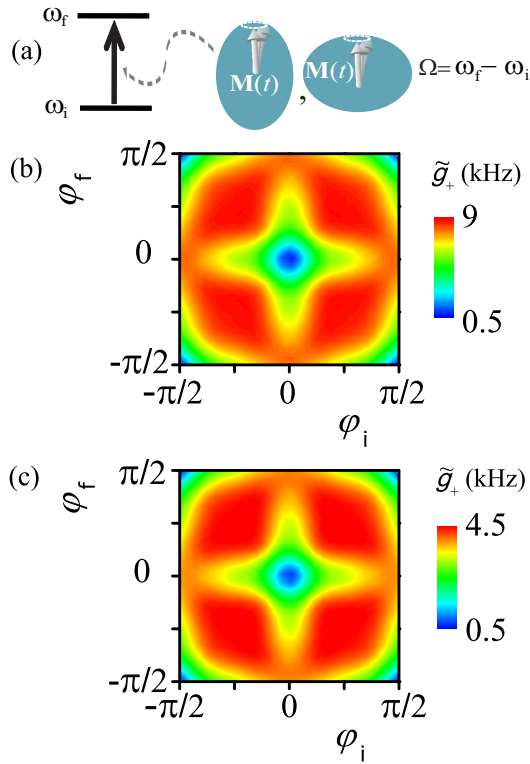


FIG. 2. (a) Schematic representation of the triple resonance condition in an optical frequency up-conversion (one-magnon absorption) process; photon transition from a mode at a state $|i\rangle = \sin \varphi_i | -m_i \rangle + \cos \varphi_i | m_i \rangle$ with angular frequency $\omega_i = \omega_{|m_i|}$ to a mode at a state $|f\rangle = \sin \varphi_f | -m_f \rangle + \cos \varphi_f | m_f \rangle$ with angular frequency $\omega_f = \omega_{|m_f|}$, by absorption of one magnon of angular frequency $\Omega = \omega_f - \omega_i$. The Kittel magnon is schematically illustrated in the prolate and oblate spheroid under consideration. (b) Color scale: magnitude of the optomagnonic coupling strength, $\tilde{g}_+ = |g_+| \epsilon_0 / \hbar$, for triple-resonant photon transitions from an initial photon state in the irreducible subspace with $|m_i| = 9$ to a final photon state in the irreducible subspace with $|m_f| = 10$ for the prolate spheroid under consideration. (c) Color scale: magnitude of the optomagnonic coupling strength, $\tilde{g}_+ = |g_+| \epsilon_0 / \hbar$, for triple-resonant photon transitions from an initial photon state in the irreducible subspace with $|m_i| = 10$ to a final photon state in the irreducible subspace with $|m_f| = 9$ for the oblate spheroid under consideration.

initial and final states that were otherwise not allowed in a sphere.

Until now we discussed YIG spheroids, although such particles with high finesse are not easily fabricated and controlled experimentally. On the other hand, cylindrical YIG samples of high quality factors lie within the reach of current micro-fabrication techniques [48–50]. The analysis of the $|m|$ -split optical modes of microcylinders follows suit of the analysis of spheroids already discussed. Let us assume a YIG microcylinder as the one shown in the inset of Fig. 3. We set the radius of the cylinder fixed at $R = 5 \mu\text{m}$ and consider three distinct values for the height h , namely, $h = 10 \mu\text{m}$, $h = 9.9 \mu\text{m}$, and $h = 9.8 \mu\text{m}$. To ensure convergence, we truncated the relevant angular-momentum expansions at $\ell_{\text{max}} = 22$ and $\ell_{\text{cut}} = 26$, and used a Gaussian quadrature integration formula with 1024 points for the integrals involved. In Fig. 3(a), we show

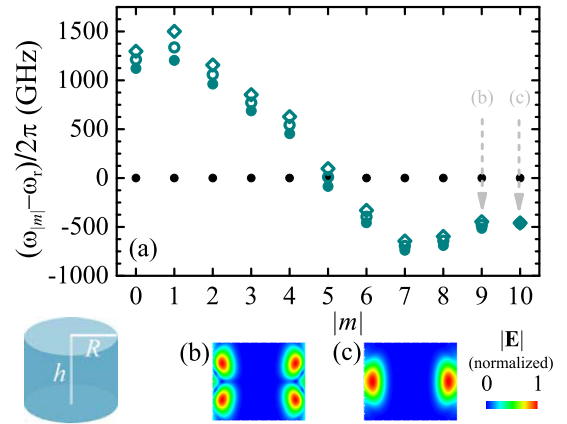


FIG. 3. (a) Cyan symbols: $|m|$ -split Mie resonance frequencies for the unmagnetized YIG cylinder with radius $R = 5 \mu\text{m}$ and height h , shown in the graphical inset, for three different values of h : $h = 10 \mu\text{m}$ (filled circles), $h = 9.9 \mu\text{m}$ (open circles), and $h = 9.8 \mu\text{m}$ (open diamonds). The black solid circles show the eigenfrequency ω_r of the corresponding degenerate Mie modes ($\text{TM}_{\ell=10, \nu=1}$) of a sphere with radius $R = 5 \mu\text{m}$, which serves as a reference for the visualization of level splitting in the GHz scale. The vertical arrows mark the $|m| = 9$ and $|m| = 10$ modes. The normalized electric-field profile of these modes in a plane cutting the cylinder along its axis are shown in (b) and (c), respectively (the intensity pattern is the same for the $\pm m$ modes).

with colored symbols the optical Mie eigenmodes of the three cylinders with different height h , while the black dots correspond to the eigenfrequency of the YIG sphere with $R = 5 \mu\text{m}$, which serves as a reference. The cyan closed symbols that correspond to $h = 10 \mu\text{m}$ exhibit a roughly symmetrical splitting with respect to the frequency of the sphere ω_r , although the modes with higher $|m|$ are slightly closer to ω_r . Note, however, that for the cylinder with $h = 10 \mu\text{m}$, contrary to the case of the spheroid (see Fig. 1), the frequency split always exceeds 50 GHz, which is much larger than the Kittel magnon frequency in that particle.

However, as shown with cyan open circles in Fig. 3(a), when the height is changed to $h = 9.9 \mu\text{m}$, almost all modes are shifted to slightly higher frequencies, with the exception of the $|m| = 10$ modes which remain roughly unchanged. This is further demonstrated for $h = 9.8 \mu\text{m}$, shown with cyan open diamonds in Fig. 3(a). The frequency difference between the $|m| = 10$ and the $|m| = 9$ modes now becomes ~ 11 GHz, which lies within the reach of the Kittel magnon frequencies. By adjusting the height h of the cylinder, this frequency difference can be finely tuned to a desired value, as confirmed by the calculation, and this can be used in a possible experimental realization. Furthermore, modes of higher $|m|$ are more easily excited in the laboratory using techniques such as evanescent coupling or scattering, since the field is mostly concentrated close to the circumference of the cylinder. In fact, in Figs. 3(b) and 3(c) we show the respective electric-field profiles for the modes $|m| = 9$ and $|m| = 10$, pointed out with arrows in 3(a), respectively. The electric field intensity is normalized to unity and is shown in a plane that cuts the cylinder along its axis. As we can see, the field in mode $|m| = 10$ should not be significantly affected by small variations of the cylinder

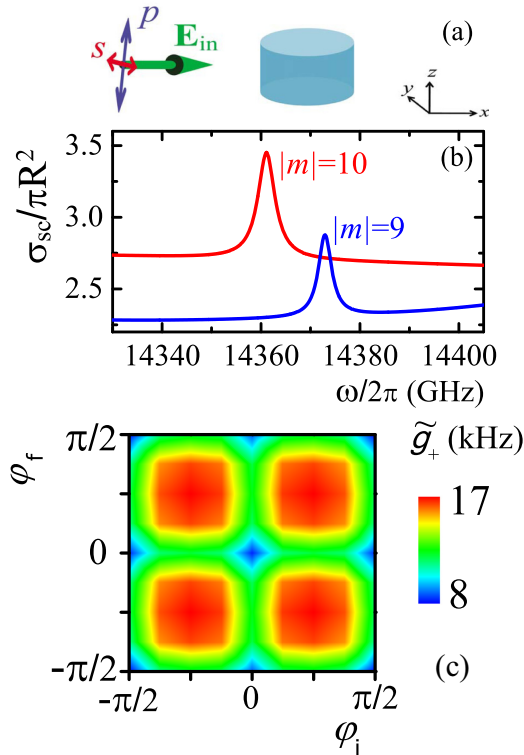


FIG. 4. (a) YIG cylinder with $R = 5 \mu\text{m}$ and $h = 9.8 \mu\text{m}$ in a scattering configuration where light impinges normally to the cylinder's axis in two possible linear polarizations, s and p . (b) Scattering cross section spectra for s and p polarized incident light. The $|m|$ subspace of the modes excited in each case is marked next to the corresponding peak. Red and blue colors denote s and p polarization of the incident light, respectively. (c) Color scale: magnitude of the optomagnonic coupling strength, $\tilde{g}_+ = |g_+| \epsilon_0 / \hbar$, for triple-resonant photon transitions from an initial state $|i\rangle = \sin \varphi_i | -m_i \rangle + \cos \varphi_i | m_i \rangle$ with $|m_i| = 10$ to a final photon state $|f\rangle = \sin \varphi_f | -m_f \rangle + \cos \varphi_f | m_f \rangle$ with $|m_f| = 9$ for the cylindrical particle under consideration.

height, since it is localized in the middle region around the circumference.

As mentioned above, the photonic eigenmodes of the cylinder can be probed, for instance, using light-scattering spectroscopy. In Fig. 4(b), we show the scattering cross section spectrum, for linearly polarized light that impinges on a cylinder with $h = 9.8 \mu\text{m}$, normally to its axis (z axis), as depicted schematically in Fig. 4(a). As expected from a group theory analysis [30], modes of the $|m| = 10$ subspace are excited by s -polarized light incident normally to the cylinder's axis, while p polarization is compatible with modes of the $|m| = 9$ subspace (all modes have even parity, $\sigma = g$). It can be seen that the two peaks are well separated and thus a triply resonant optical transition is feasible. Selection rules and energy conservation allow only two possible magnon-mediated transitions: from $|m_i| = 10$ to $|m_f| = 9$ through a respective magnon absorption and from $|m_i| = 9$ to $|m_f| = 10$ through a respective magnon emission. As evident also from Fig. 3(b), both transitions are nonreciprocal, i.e., a resonant magnon absorption (emission) is not accompanied by a respective magnon emission

(absorption). This property might be important in view of magnon cooling/heating applications [40,51,52]. Again, to first order in perturbation theory, we can calculate the optomagnonic coupling strengths g_{\pm} by integrating over the volume of the cylinder. Spin wave normalization, expressed by Eq. (9), yields $\eta \simeq 5.8 \times 10^{-7}$. Exploring optical transitions from the $|m_i| = 10$ to the $|m_f| = 9$ subspace, we obtain a maximum optomagnonic coupling strength of $\tilde{g}_+ \simeq 17 \text{ kHz}$, as shown in Fig. 4(c). It is worth noting that, although in the cases considered here the optical modes involved are in the far-infrared part of the spectrum, extension to different spectral regions is possible by properly adjusting the size and geometry of the particle.

Typical experimental works focus on larger particles, in the (sub)millimeter scale, where the triple-resonance condition is met between successive optical WGMs, while the measured optomagnonic coupling strength is of the order of Hz [24–26]. Similarly, theoretical studies predict that the spin wave amplitude η for millimeter sized spheres is of the order of 10^{-9} . By shrinking the size of the particles to few micrometers, $\eta \approx 10^{-6}$ [see Eq. (9)], so our calculations predict a three orders of magnitude increase of the photon magnon coupling strength for micrometer-sized particles, along with a further 10-fold enhancement due to the nonsphericity [see, e.g., Figs. 2(b) and 2(c)]. However, although here the optomagnonic coupling strength is significantly increased compared to spherical YIG resonators, the fact that \tilde{g}_{\pm} is smaller than both γ_K and γ_V indicates that we are still in the weak coupling regime.

V. CONCLUSIONS

In summary, we studied the strengthening of the optomagnonic interaction in nonspherical axisymmetric YIG microparticles and derived the respective selection rules for magnon-mediated optical transitions between optical Mie modes based on group theory. Such triply resonant interactions can be handily engineered by exploiting the extra degree of freedom provided by the shape anisotropy of nonspherical resonators. In the framework of the first-order Born approximation, we calculated the transition amplitudes for oblate and prolate spheroidal as well as cylindrical particles. The initial and final optical states have been calculated using the EBCM for scatterers with axial symmetry. Our results predict enhanced optomagnonic coupling strengths of the order of tens of kHz in undoped YIG cylindrical microparticles, which is several orders of magnitude larger compared to that obtained in (sub)millimeter YIG spheres. Our findings elucidate the implications and benefits from the symmetry lowering of the particle shape and predict that, while the reduction of volume is the major effect for micron-sized particles, a further, almost 10-fold, interaction enhancement is obtained by deviating from the spherical shape.

ACKNOWLEDGMENTS

E.A. acknowledges support for this research, which is cofinanced by Greece and the European Union [European Social Fund (ESF)] through the Operational Programme ‘‘Human Resources Development, Education and

Lifelong Learning” in the context of the project “Reinforcement of Postdoctoral Researchers, 2nd Cycle” (No. MIS-

5033021), implemented by the State Scholarships Foundation (IKY).

-
- [1] P. Dong, Y. K. Chen, G. H. Duan, and D. T. Neilson, *Nanophotonics* **3**, 215 (2014).
- [2] D. Thomson, A. Zilkie, J. E. Bowers, T. Komljenovic, G. T. Reed, L. Vivien, D. Marris-Morini, E. Cassan, L. Virost, J.-M. Fédéli, J.-M. Hartmann, J. H. Schmid, D.-X. Xu, F. Boeuf, P. O’Brien, G. Z. Mashanovich, and M. Nedeljkovic, *J. Opt.* **18**, 073003 (2016).
- [3] A. V. Chumak, V. I. Vasyuchka, A. A. Serga, and B. Hillebrands, *Nat. Phys.* **11**, 453 (2015).
- [4] V. V. Kruglyak *et al.*, in *Magnonic Metamaterials*, edited by X.-Y. Jiang (InTech, London, 2012).
- [5] D. Zhang, X.-Q. Luo, Y.-P. Wang, T.-F. Li, and J. Q. You, *Nat. Commun.* **8**, 1368 (2017).
- [6] J. Walowski and M. Münzenberg, *J. Appl. Phys.* **120**, 140901 (2016).
- [7] Z. Zhang, M. Vogel, J. Holanda, M. B. Jungfleisch, C. Liu, Yi Li, J. E. Pearson, R. Divan, W. Zhang, A. Hoffmann, Y. Nie, and V. Novosad, *Appl. Phys. Lett.* **115**, 232402 (2019).
- [8] R. Hisatomi, A. Osada, Y. Tabuchi, T. Ishikawa, A. Noguchi, R. Yamazaki, K. Usami, and Y. Nakamura, *Phys. Rev. B* **93**, 174427 (2016).
- [9] N. J. Lambert, A. Rueda, F. Sedlmeir, and H. G. Schwefel, *Adv. Quantum Technol.* **3**, 1900077 (2020).
- [10] D. Lachance-Quirion, Y. Tabuchi, A. Gloppe, K. Usami, and Y. Nakamura, *Appl. Phys. Express* **12**, 070101 (2019).
- [11] V. A. S. V. Bittencourt, V. Feulner, and S. V. Kusminskiy, *Phys. Rev. A* **100**, 013810 (2019).
- [12] *Optomagnonic Structures: Novel Architectures for Simultaneous Control of Light and Spin Waves*, edited by E. Almpanis (World Scientific, Singapore, 2021).
- [13] M. Kostylev and A. A. Stashkevich, *J. Magn. Magn. Mater.* **484**, 329 (2019).
- [14] N. Zhu, X. Zhang, X. Han, C. L. Zou, C. Zhong, C. H. Wang, L. Jiang, and H. Tang, *Optica* **7**, 1291 (2020).
- [15] J. W. Kłós, M. Krawczyk, Y. S. Dadoenkova, N. N. Dadoenkova, and I. L. Lyubchanskii, *J. Appl. Phys.* **1115**, 174311 (2014).
- [16] J. W. Kłós, I. L. Lyubchanskii, M. Krawczyk, P. Gruszecki, S. Mieszczak, J. Rychły, Y. S. Dadoenkova, and N. N. Dadoenkova, Magnonics and confinement of light in photonic-magnonic crystals, in *Optomagnonic Structures: Novel Architectures for Simultaneous Control of Light and Spin Waves* (World Scientific, Singapore, 2021).
- [17] T. Y. Liu, X. F. Zhang, H. X. Tang, and M. E. Flatté, *Phys. Rev. B* **94**, 060405(R) (2016).
- [18] P. A. Pantazopoulos, N. Stefanou, E. Almpanis, and N. Papanikolaou, *Phys. Rev. B* **96**, 104425 (2017).
- [19] M. A. Kozhaev, A. I. Chernov, D. A. Sylgacheva, A. N. Shaposhnikov, A. R. Prokopov, V. N. Berzhansky, A. K. Zvezdin, and V. I. Belotelov, *Sci. Rep.* **8**, 11435 (2018).
- [20] P. A. Pantazopoulos and N. Stefanou, *Phys. Rev. B* **99**, 144415 (2019).
- [21] P. A. Pantazopoulos, K. L. Tsakmakidis, E. Almpanis, G. P. Zouros, and N. Stefanou, *New J. Phys.* **21**, 095001 (2019).
- [22] V. A. Ozerov, D. A. Sylgacheva, M. A. Kozhaev, T. Mikhailova, V. N. Berzhansky, M. Hamidi, A. K. Zvezdin, and V. I. Belotelov, *J. Magn. Magn. Mater.* **543**, 168167 (2022).
- [23] J. Graf, S. Sharma, H. Huebl, and S. V. Kusminskiy, *Phys. Rev. Research* **3**, 013277 (2021).
- [24] A. Osada, R. Hisatomi, A. Noguchi, Y. Tabuchi, R. Yamazaki, K. Usami, M. Sadgrove, R. Yalla, M. Nomura, and Y. Nakamura, *Phys. Rev. Lett.* **116**, 223601 (2016).
- [25] X. Zhang, N. Zhu, C.-L. Zou, and H. X. Tang, *Phys. Rev. Lett.* **117**, 123605 (2016).
- [26] J. A. Haigh, A. Nunnenkamp, A. J. Ramsay, and A. J. Ferguson, *Phys. Rev. Lett.* **117**, 133602 (2016).
- [27] C. Kittel, *Phys. Rev.* **73**, 155 (1948).
- [28] E. Almpanis, *Phys. Rev. B* **97**, 184406 (2018).
- [29] E. Almpanis, G. P. Zouros, P. A. Pantazopoulos, K. L. Tsakmakidis, N. Papanikolaou, and N. Stefanou, *Phys. Rev. B* **101**, 054412 (2020).
- [30] G. Gantzounis, *J. Phys. Chem. C* **113**, 21560 (2009).
- [31] M. I. Mishchenko, L. D. Travis, and A. A. Lacis, *Scattering, Absorption, and Emission of Light by Small Particles* (Cambridge University Press, Cambridge, UK, 2002).
- [32] G. Gantzounis and N. Stefanou, *Phys. Rev. B* **73**, 035115 (2006).
- [33] C. Tserkezis, N. Papanikolaou, E. Almpanis, and N. Stefanou, *Phys. Rev. B* **80**, 125124 (2009).
- [34] E. Almpanis, P.-A. Pantazopoulos, N. Papanikolaou, V. Yannopoulos, and N. Stefanou, *J. Opt. Soc. Am. B* **33**, 2609 (2016).
- [35] T. Inui, Y. Tanabe, and Y. Onodera, *Group Theory and its Applications in Physics* (Springer-Verlag, Berlin, 1990).
- [36] D. D. Stancil and A. Prabhakar, *Spin Waves-Theory and Applications* (Springer, Boston, 2009).
- [37] G. P. Zouros, G. D. Kolezas, N. Stefanou, and T. Wriedt, *IEEE Trans. Antennas Propag.* **69**, 6134 (2021).
- [38] A. Osada, A. Gloppe, R. Hisatomi, A. Noguchi, R. Yamazaki, M. Nomura, Y. Nakamura, and K. Usami, *Phys. Rev. Lett.* **120**, 133602 (2018).
- [39] S. Sharma, B. Z. Rameshti, Y. M. Blanter, and G. E. W. Bauer, *Phys. Rev. B* **99**, 214423 (2019).
- [40] S. V. Kusminskiy, Cavity optomagnonics, in *Optomagnonic Structures: Novel Architectures for Simultaneous Control of Light and Spin Waves* (World Scientific, Singapore, 2021).
- [41] J. Graf, H. Pfeifer, F. Marquardt, and S. Viola Kusminskiy, *Phys. Rev. B* **98**, 241406(R) (2018).
- [42] G. C. Stangle, K. R. Venkatachari, S. P. Ostrander, W. A. Schulze, and J. D. Pietras, US Patent No. 5,660,773 (1997).
- [43] M. Jafelicci, Jr. and R. H. M. Godoi, *J. Magn. Magn. Mater.* **226**, 1421 (2001).
- [44] F. Grasset, S. Mornet, A. Demourgues, J. Portier, J. Bonnet, A. Vekris, and E. Duguet, *J. Magn. Magn. Mater.* **234**, 409 (2001).
- [45] C. L. Sones, M. Feinaeugle, A. Sposito, B. Gholipour, and R. W. Eason, *Opt. Express* **20**, 15171 (2012).

- [46] T. Schmitz, U. Wiedwald, C. Dubs, and B. Gökce, *ChemPhysChem* **18**, 1125 (2017).
- [47] M. Kuwata-gonokami, K. Ema, and K. Takeda, *Mol. Cryst. Liq. Cryst.* **216**, 21 (1992).
- [48] S. R. Compton, Master thesis, University of Alberta, 2012.
- [49] Z. Diao, J. E. Losby, J. A. J. Burgess, V. T. K. Sauer, W. K. Hiebert, and M. R. Freeman, *J. Vac. Sci. Technol. B* **31**, 051805 (2013).
- [50] *Three-Dimensional Magnonics: Layered, Micro- and Nanostructures*, edited by G. Gubbiotti (CRC Press, Boca Raton, FL, 2019).
- [51] S. Sharma, Y. M. Blanter, and G. E. W. Bauer, *Phys. Rev. Lett.* **121**, 087205 (2018).
- [52] F. Šimić, S. Sharma, Y. M. Blanter, and G. E. W. Bauer, *Phys. Rev. B* **101**, 100401(R) (2020).